Fuel 215 (2018) 844–852

Contents lists available at ScienceDirect

Fuel

journal homepage: www.elsevier.com/locate/fuel

Full Length Article

Coal permeability: Gas slippage linked to permeability rebound

Yufu Niu, Peyman Mostaghimi, Igor Shikhov, Zhixi Chen, Ryan T. Armstrong*

School of Petroleum Engineering, The University of New South Wales, NSW 2052, Australia

ARTICLE INFO

Keywords:
Coal permeability
Gas slippage
Permeability rebound
Slip length
Knudsen number

ABSTRACT

The main factors/mechanisms that influence coal permeability are effective stress, swelling, shrinkage, deformation and gas slippage. After an extended period of gas production, coal can have a rebound phenomenon where permeability increases with increasing effective stress. This rebound can have a significant impact on gas recovery during the late stages of a reservoir life cycle. This paper aims to characterise coal permeability by combining laboratory measurements with a simple gas slippage model that explains the rebound phenomenon. Gas and Klinkenberg corrected permeabilities of coal are measured at (1) constant confining pressure and (2) constant effective stress. We estimate the length scales relevant to gas flow using mercury intrusion, a permeability slip model, and the kinetic theory of gases, which allows us to estimate the Knudsen number for gas flow. Results show a linear relationship between slip length and the mean free path of gas for all of the tested mean pore pressures. This result suggests that a first order slip boundary condition is sufficient to explain the momentum exchange at the gas/solid boundary during flow under normal reservoir conditions. A correlation between Knudsen number and increased permeability is developed, which further demonstrates that slippage cannot be neglected in coals when Knudsen number is greater than 0.1. Overall, we present a simple model that explains permeability rebound in coal by considering only gas slippage. We do not discredit the mechanism of coal shrinkage, which could also influence coal permeability. We confirm that gas slippage should be considered in coal permeability models.

1. Introduction

Coal bed methane is a significant unconventional resource for natural gas. During methane production and/or CO_2 storage in coal beds, a primary parameter to evaluate production and/or injection rate is permeability. Unlike sandstone and carbonate reservoirs, coal permeability is highly dependent on reservoir parameters [52,17,50,40,35]. Coal is deformable and thus, increasing effective stress can drastically reduce permeability. In addition, coal is known to shrink as gas is desorbed, which could influence its pore volume and permeability. Lastly, the characteristic length scales associated with the internal structure of coal are often comparable to the mean free path of methane gas and thus, gas slippage is a relevant flow mechanism. However, current coal permeability models often consider only the mechanical effects and often overlook the influence of gas slippage.

Coal is composed of matrix and cleats, which are denoted as face and butt cleats. These cleats are normal to the bedding plane and perpendicular to each other [7,42,26,37]. Coal permeability is influenced by a series of cleat characteristics including size, spacing, connectivity, filled mineral and orientation patterns [26,40,22,22]. Coal permeability has been evaluated widely based on various effective stresses and matrix shrinkage studies [52,14,19,19,41,5,21,34,29,56]. These studies have concluded that coal permeability in higher permeability (100 mD) samples can decrease a full order of magnitude when increasing effective stress whereas lower permeability (1 mD) coal samples can decrease over two orders of magnitude. They have also concluded that coal permeability increases with decreasing pore pressure due to a mechanism commonly referred to as shrinkage. While gas slippage may also play a role it has been suggested that the effect of gas slippage is relatively small compared with the shrinkage effect at intermediate pore pressures around 10–25 MPa [9]. However, how shrinkage actually influences cleat aperture sizes and cleat network topology has yet to be shown experimentally. To verify the contribution of the slippage effect on coal permeability, the length scales associated with gas slippage and those relevant to the coal structural morphology must be considered. In addition, laboratory studies have found that coal permeability with adsorbed gas such as methane is lower than permeability with inert gases such as helium because of the swelling effect that occurs when methane gas is adsorbed to the coal matrix. Overall, the coupling between coal mechanics, swelling, and slippage has yet to be fully explained in coal permeability models.

One of the first coal permeability models was proposed by Gray

* Corresponding author.
E-mail address: Ryan.Armstrong@unsw.edu.au (R.T. Armstrong).

https://doi.org/10.1016/j.fuel.2017.11.082
Received 7 September 2017; Received in revised form 21 November 2017; Accepted 22 November 2017

[17], which considered various effective stresses and matrix shrinkage with desorption. The relationship between shrinkage strain and sorption pressure was built by considering an elastic relation between stress and strain. Sawyer et al. [47] demonstrated a 3D coal bed model, which was built by considering the correlation between matrix compressibility and adsorbed gas amount. They illustrated that the shrinkage effect of coal can offset the effective stress from cleat shrinkage related to pore volume compaction. However, a systematic coal permeability model was not developed until the matchstick geometry model, which was first built by Reiss [44]. Based on the matchstick geometry, Seidle et al. [49] derived a permeability equation with matrix shrinkage, hydrostatic stress and laboratory results using uniaxial stress condition. This model was further developed by Shi and Durucan [51] to address the impact of matrix shrinkage and swelling with the assumption that permeability varies exponentially with horizontal effective stress. Palmer and Mansoori [39] built a popular permeability model to correlate permeability with stress and pore pressure by assuming uniaxial strain and constant vertical stress. In addition, many other researchers developed permeability models for coal by considering stress-induced matrix shrinkage [28,39,43,8,50,45,8,31,30,57]. But only a few developed models consider gas slippage [18,18,16,56].

This paper examines coal permeability based on the coupling of gas slippage and matrix deformation. We exclude the effect of matrix shrinkage by using helium gas, which does not undergo sorption to coal. Two conditions are considered in this paper: (1) constant confining pressure and (2) constant effective stress. We conclusively show that permeability rebound can occur in the absence of coal shrinkage. The results demonstrate that coal permeability models should account for both gas slippage and shrinkage. A simple permeability model using the Maxwell slippage boundary condition [33] is developed to explain permeability rebound observed with helium gas. We provide a detailed analysis of the length scales involved, boundary conditions required to model the physics, and provide conceptual insights into coal permeability rebound. Our model and experimental data demonstrate that permeability rebound due to gas slippage is most prevalent in coals with permeabilities less than 1 mD and at pore pressures approaching the expiration of a coal seam.

2. Materials and methods

The experimental setup is displayed in Fig. 1. The coal samples are 6 cm in diameter and of various lengths from 3.70 cm to 9.65 cm, which are placed in a triaxial core holder and hydrostatic confining pressure is applied. Two high-precision transducers of maximum 1000 psig and 100 psig with precision of 0.08% are used to measure the inlet and outlet pressure. Flow rate is measured three to five times by a Ruska gasometer and measured values are averaged to calculate permeability. A backpressure regulator is installed at the outlet to keep the pressure drop over the sample limited to 40 psig for all experiments. Controlling the pressure drop is critical for gas experiments with coal since coal is highly deformable and gases can exhibit large pressure drops. A large pressure drop would make it difficult to interpret the results since effective stress would change along the cores length and thus, average values for the experiment would not be representative.

The volumetric flow rate for gas varies along the core due to compressibility. Following Darcy's law and applying the ideal gas law, the gas permeability is measured as

$$K_{g=}\frac{2QP_a\mu L}{0.001127A\left(P_1^2-P_2^2\right)} \tag{1}$$

where P_a is atmosphere pressure, Q is flow rate measured at P_a, μ is viscosity, L is sample length, A is area, P_1 is inlet pressure and P_2 is outlet pressure [48]. To determine the samples Klinkenberg corrected permeability, we follow the work of Klinkenberg [25] where it was proposed that gas permeability (K_g) is a linear function of the reciprocal mean pore pressure ($\overline{p}$), defined as

$$\frac{K_g}{K} = 1 + \frac{b}{\overline{p}} \tag{2}$$

$$\overline{p} = \frac{P_1 + P_2}{2} \tag{3}$$

where K is absolute (Klinkenberg corrected) permeability and b is the Klinkenberg coefficient. Here, $\overline{p}$ is related to the characteristic length scale as

$$\frac{b}{\overline{p}} = 4c\frac{\lambda}{r} \tag{4}$$

where λ is the mean free path for gas, r is the characteristic system size and c is a proportionality factor. The parameters b and c must be determined empirically for a given gas and rock combination. The mean free path of a gas can be determined from the kinetic theory of gases, defined as

$$\lambda = \frac{k_B T}{\sqrt{2}\pi d^2 p} \tag{5}$$

where k_B is the Boltzmann constant, T is absolute temperature, d is cross-sectional diameter of the gas molecule and p is pressure [4].

From Eq. (2), when gas permeability is plotted verse $1/\overline{p}$, the apparent gas permeability extrapolated to infinite pressure provides a constant permeability without the effects of slippage. This concept is utilised to determine the Klinkenberg corrected permeability of our samples by plotting gas permeability versus $1/\overline{p}$ for constant effective stress with variable mean pore pressure. The resulting extrapolated permeability value is the Klinkenberg corrected permeability of the coal samples at a given effective stress.

Three coal samples are considered, which we refer to as low (0.05–0.25 mD), intermediate (1.5–2.2 mD) and high permeability (6–8.5 mD). One sandstone sample is also used as a control, which is relatively non-deformable and has permeability in range of 0.5–1.5 mD that is in the same order of magnitude as the coal samples. The coal samples are from Gloucester Basin, New South Wales, Australia and the tight sandstone sample is from Camden South, New South Wales, Australia. Images of the inlet and outlet faces of all samples are displayed in Fig. 2. Coal is a brittle material and it is nearly impossible to get a core sample without some degree of damage. There are damaged regions along the perimeter of the samples, where we apply blue tack to fill the gaps between the rubber sleave and sample. This is required to prevent gas flow along the cores perimeter, i.e. between the sleeve and core.

Two experimental conditions are used: (1) constant confining pressure and (2) constant effective stress. Condition (1) is applied to mimic the production process. The inlet pressure decreases from 140 psig to 10 psig (Effective stress increases from 80 psig to 195 psig) and the outlet pressure, which is controlled by a backpressure regulator decreases from 100 psig to 0 psig. Following the work of Terzaghi [53], the effective stress is defined as:

$$\sigma_e = \sigma_a - \alpha\overline{p} \tag{6}$$

where σ_e is effective stress, σ_a is confining pressure, α is Biot number and $\overline{p}$ is mean pore pressure [53]. While $\alpha = 1$ is not necessarily the case for coal, the assumption is valid since we only compare trends between similar samples and thus we only need constant/similar values of α for the comparison. For Condition (2), we maintain constant effective stress by increasing/decreasing both pore pressure and confining pressure at the same time. The range of pressures used for Condition (2) is the same as that used for Condition (1). This allows us to remove the influence of matrix deformation and thus, study gas slippage independently. According to the changing mean pore pressure at constant effective stress; we are able to apply the Klinkenberg correction to determine the theoretical Klinkenberg corrected permeability for each effective stress.

Fig. 1. Permeability experiment scheme (①: Helium cylinder; ②: Helium pressure regulator; ③: Hand pump for confining pressure; ④: Inlet pressure transducer; ⑤: Triaxial core holder; ⑥: Pressure gauge for confining pressure; ⑦: Outlet pressure transducer; ⑧: Back pressure regulator; ⑨: Pressure display monitor; ⑩: Gas flow meter).

3. Model development

We derive a simple model for gas slippage through a capillary tube starting from the Navier-Stokes equation and applying a first order slip boundary condition. While coal is a complex structure of fractures and porous matrix, it is likely that core-scale permeability is controlled by only a few of the largest pores/fractures, as demonstrated in other porous materials [46]. Therefore, we assume that a simple capillary tube model with a single length scale can capture the permeability of coal in core-scale experiments. The entire model derivation is provided for completeness. When fluid flows pass a solid wall under a no-slip boundary condition, the tangential velocity at the wall is considered as zero [12]. However, non-zero tangential velocity can occur with the flow of a gas, which is denoted to as the slip velocity v_{slip} [61] and is defined as

$$v_{slip} = b_1 \frac{\partial v(r)}{\partial r}\bigg|_{r=R} \tag{7}$$

where b_1 is the slip length, R is pipe radius, $v(r)$ is tangential velocity [36,10,55,10,2]. The slip length (b_1) is a well-defined parameter that characterises the fictitious depth into the capillary tube wall that would bring the velocity profile to a value of zero. Based on the original works of Maxwell on the kinetic theory of gases, it was shown that the slip length (b_1) has a linear relationship with mean free path length. This expression is defined as

$$b_1 = \frac{2-\sigma_v}{\sigma_v}\lambda = c\lambda \tag{8}$$

where λ is the mean free path length, σ_v is the tangential momentum accommodation coefficient (TMAC) that represents the mean exchange rate of molecules at the surface boundary [58,59]. The proportionality constant $c = (2-\sigma_v)/\sigma_v$ is often referred to as the slip constant. The boundary condition defined in Eqs. (7) and (8) is known as the Maxwell slip boundary condition and its application is often limited to low Knudsen numbers, i.e. $Kn \leqslant 0.1$ [24]. Knudsen number is defined as

$$Kn = \frac{\lambda}{r_e} \tag{9}$$

where λ is mean free path length and r_e is characteristic length scale, which can be considered as the capillary radius (R = r_e) in the proposed model.

Based on the Navier-Stokes equation, the flow equation in a pipe applying cylindrical coordinates is expressed as

$$-\frac{\partial p}{\partial z} + \mu\frac{1}{r}\frac{\partial}{\partial r}\left(r\frac{\partial v_z}{\partial r}\right) = 0 \tag{10}$$

where r is pipe radius, z is axis direction [12,2]. By integrating r, Eq. (10) is further derived as

$$\int_0^r \frac{\partial}{\partial r}\left(r\frac{\partial v_z}{\partial r}\right) = \int_0^r \frac{1}{\mu}\frac{\partial p}{\partial z}r \tag{11}$$

$$\frac{\partial v_z}{\partial r} = \frac{1}{\mu}\frac{\partial p}{\partial z}\frac{r}{2} + C_1 \tag{12}$$

We then apply a symmetry boundary condition that $\frac{\partial v}{\partial r} = 0$ at $r = 0$ (the tubes center), such that $C_1 = 0$, then further integration results in

$$v_z(r) = \frac{1}{\mu}\frac{\partial p}{\partial z}\frac{r^2}{4} + C_2 \tag{13}$$

Applying the slip boundary condition from Eq. (7) to Eq. (12) at $r = R$ and combine with Eq. (13) at $r = R$, C_2 can be determined as

$$v_{z|r=R} = \frac{1}{\mu}\frac{\partial p}{\partial z}\frac{R^2}{4} + C_2 = v_z|_{r=R} = v_{slip} = -b_1\frac{\partial v_z}{\partial r}\bigg|_{r=R} = -\frac{b_1}{\mu}\frac{\partial p}{\partial z}\frac{R}{2} \tag{14}$$

$$C_2 = -\frac{1}{\mu}\frac{\partial p}{\partial z}\left(\frac{R^2}{4} + \frac{Rb_1}{2}\right) \tag{15}$$

By inserting C_2 into Eq. (13), the velocity profiles $v_z(r)$ expression [54] is defined as

$$v_z(r) = -\frac{1}{\mu}\frac{R^2}{4}\frac{\partial p}{\partial z}\left(1-\frac{r^2}{R^2} + \frac{2b_1}{R}\right) \tag{16}$$

Lastly the flux Q can be obtained by integrating $v_z(r)$ from Eq. (16) for the tube cross section [27] which is expressed as

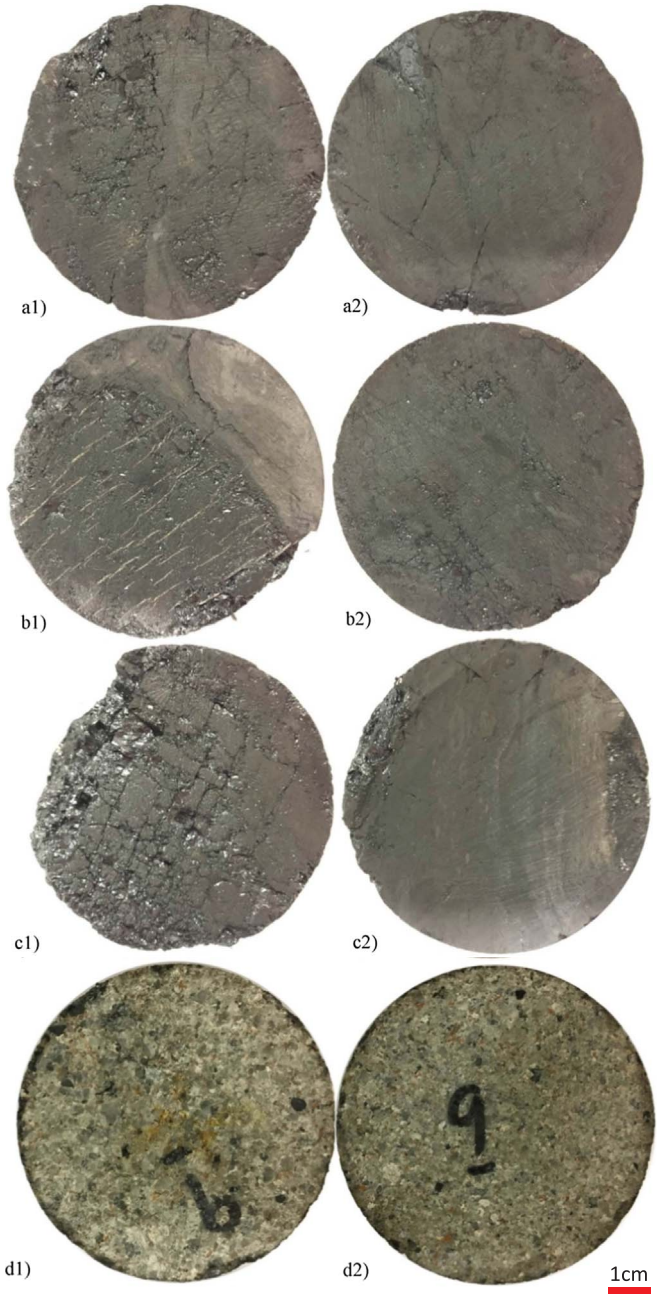

Fig. 2. Overview of the experimental samples ([a1–a2]: Low permeable coal top and bottom; [b1–b2]: Intermediate permeable coal top and bottom; [c1–c2]: High permeable coal top and bottom; [d1–d2]: Sandstone top and bottom).

$$Q = \int_0^R 2\pi r v_z(r)dr = -\frac{\pi R^4}{8}\frac{\partial p}{\partial z}\left(1 + \frac{4b_1}{R}\right) \tag{17}$$

If the tube radius (R) in Eq. (17) is large, we then have the standard Hagan-Poiseuille equation for flow through a tube and thus, the influence of gas slippage is negligible. Therefore, the flux without gas slippage is defined as

$$Q_0 = \int_0^R 2\pi r v_z(r)dr = -\frac{\pi R^4}{8}\frac{\partial p}{\partial z} \tag{18}$$

where Q_0 is the flux. Then dividing Eq. (17) by Eq. (18), we obtain

$$\frac{Q}{Q_0} = 1 + \frac{4b_1}{R} \tag{19}$$

To relate Eq. (19) to laboratory permeability measurements, the ratio of gas permeability and Klinkenberg corrected permeability based on Darcy's law for Q/Q_0 is defined as

$$\frac{K_g}{K_l} = 1 + \frac{4b_1}{R} \tag{20}$$

where K_g is apparent gas permeability, K_l is Klinkenberg corrected permeability without slippage and $R = r_e$ the characteristic length scale.

Eq. (20) is useful since it relates the ratio between gas and Klinkenberg corrected permeabilities to the ratio between the slippage length (b_1) and a characteristic length scale (r_e). In addition, the results are analogous to Klinkenberg [25] as discussed in Section 2 for determining gas and Klinkenberg corrected permeability.

We consider the result of Eq. (20) by plotting K_g/K_l versus R at a given mean pore pressure using our 4 different permeability samples to provide a range of characteristic length scales (r_e). The free parameter is slippage length (b_1), which we adjust to best fit the experimental data using regression analysis. For this purpose the characteristic physical length scale of the porous samples are estimated as

$$r_e \approx 5\sqrt{K/ø} \tag{21}$$

where K is absolute permeability and ø is porosity [13]. In addition, to estimate porosity and length scales, mercury intrusion data is applied. In this way, we can estimate the characteristic length scale of the samples by Eq. (21) and substantiate our results with mercury intrusion data. Coal porosity is estimated by Mercury intrusion measurements while sandstone porosity is calculated as

$$ø = 1 - \frac{\rho_b}{\rho_s} \tag{22}$$

where ρ_b is bulk density, ρ_s is solid density, which is assumed as quartz density (2.65 g/cm^3).

4. Mercury intrusion measurements

Mercury intrusion porosimetry (MIP) is a frequently used method to determine the porosity and effective pore size distribution (PSD) of coals. However, MIP data require thorough corrections to conformance, thermal expansion and matrix compressibility effects. An excellent review of MIP procedures, considerations, and potential errors is provided by Comisky et al. [6]. Further accounts on the procedures and on magnitude of the compressibility effect associated with MIP measurements on coals are given by Li et al. [30] and Okolo et al. [38].

MIP measurements are performed on dried (not crushed) samples using a Quantachrome PoreMaster PM33-17. Samples of an average volume of about 0.7 cm^3 and a penetrometer with a stem volume of 0.5 cm^3 are used in these experiments. The samples sealed in a glass penetrometer are first evacuated via a low-pressure port to < 15 μm Hg for 20 min. Then the step-wise increasing pressure of up to 50 psia versus intruded mercury volume is recorded. A high-pressure hydraulic station is then used to inject mercury to approximately 33,000 psi. The PSD can be calculated using the empirical Washburn [58] equation as

$$P_{Hg} = \frac{-2\sigma cos\theta}{R} \tag{23}$$

for mercury/solid systems the default contact angle of θ = 140° and mercury surface tension σ = 480 dynes/cm are used. MIP-based characteristic length (r_e) controlling transport in the cleat network is defined as a mean radius of PSD truncated below 100 nm since smaller pore sizes would have little contribution to bulk permeability. Therefore to determine r_e, we measure average aperture size for all pores greater than 100 nm in size. The coal samples are not affected by matrix compressibility for pore sizes in the range of 0.7–2 μm since applied pressures are relatively low. We will demonstrate the applicability of our approach by comparing r_e from MIP to r_e from Eq. (21).

5. Results and discussion

5.1. Permeability analysis

A sandstone sample and three coal samples are measured for gas and Klinkenberg corrected permeability by helium gas. Hydrostatic pressure is applied laterally around the sample as confining pressure. Constant confining pressure is applied to measure gas permeability under various mean pore pressure from 135 psig to 20 psig. The relative effective stress varies from 80 to 195 psig. This range of measurements is within the range of pore pressures experienced in a CBM reservoir near the completion of its production. Well shutoff pressures are approximately 40–60 psig. With decreasing mean pore pressure the effect of gas slippage becomes stronger because the mean free path of the gas approaches the characteristic length scale of the coal structure. Consequently, gas permeability increases with diminishing mean pore pressure. Meanwhile, lower mean pore pressure means higher effective stress resulting in a reduction of cleat aperture size. As a result, gas permeability decreases by increasing effective stress. These two antagonistic effects are critical in determining what permeability trend is measured when effective stress is increased.

In Fig. 3, we demonstrate that the permeability for all of the tested samples rebounds at high effective stress. The triangular data points represent gas permeability measured by helium while the square data points represent the Klinkenberg corrected permeability. To measure the Klinkenberg corrected permeability at each effective stress, the confining pressure and mean pore pressure are increased simultaneously while keeping the effective stress constant. Then the Klinkenberg corrected permeability can be estimated using the Klinkenberg correction described in Eq. (2).

Because of the gas slippage effect, gas permeability is greater than Klinkenberg corrected permeability for all of the measured mean pore pressures, which is seen in Fig. 3. It is also observed that while Klinkenberg corrected permeability decreases with increasing effective pressure the gas permeability eventually increases at high effective stress. As noted by Arabjamaloei and Ruth [1], the concept of viscosity used to determine gas permeability becomes invalid as the system size approaches the mean free path of the gas molecules. The manifestation of this mechanism is that gas permeability increases. The effective stress at which this occurs is dependent on the specific sample tested. As seen in Fig. 3, the low permeability coal and sandstone display an increase in gas permeability around an effective stress of 130 psi whereas the higher permeability samples do not have increased gas permeability until an effective stress of around 200 psi. For the higher permeability samples an increase in effective stress initially decreases the gas permeability since the matrix is deforming and flow pathways decrease in size. However, this decrease in size has yet to reach the mean free path of the gas molecules. While in the lower permeability samples, when effective stress is increased the structure of the sample becomes smaller in size than the mean free path of gas and thus, permeability increases. We will further confirm these observations when looking at the characteristic lengths scales.

Fig. 4 shows the permeability contour plots generated by plotting pore pressure versus confining pressure. The contour plots show that coal permeability changes with changes in either pore or confining pressure while sandstone permeability changes mostly by only changes in pore pressure. This highlights the observation that while slippage occurs in both coal and sandstone; the influence of matrix deformation is mostly prevalent in coal. In addition, from Fig. 3 we can see that the low permeable coal has the largest difference between gas permeability and Klinkenberg corrected permeability at high effective stress and this difference becomes less for the medium and high permeable coal. The behaviour would suggest that the aperture size of the low permeable coal is closer to the gas mean free path length than that for the high permeable coal and that the influence of matrix deformation is less for the low permeable coal sample. This is most evident in Fig. 4 where permeability is more influenced by pore pressure than confining pressure for lower permeable coal sample while higher permeable coal

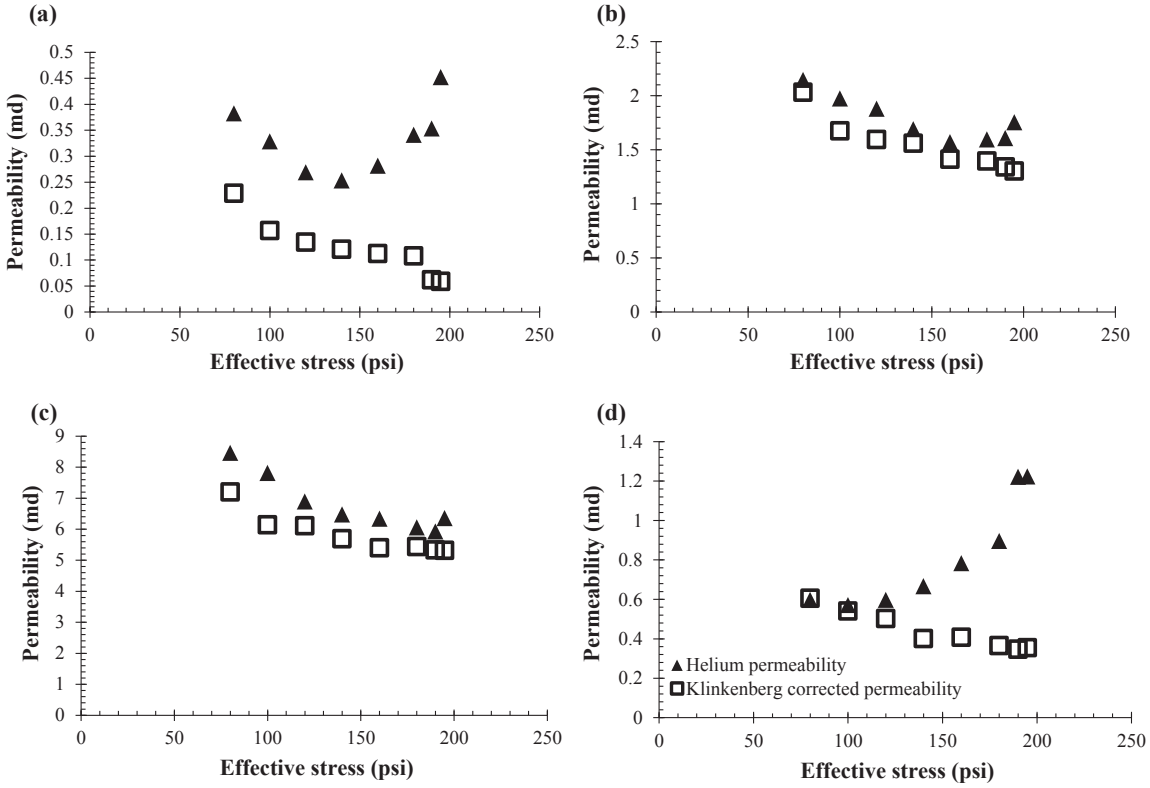

Fig. 3. Permeability rebound under constant confining pressure ([a]: low permeable coal; [b]: intermediate permeable coal; [c]: high permeable coal; [d]: sandstone. The experimental data are averaged based on 3–5 flow rate measurements and all errors are less than 10%).

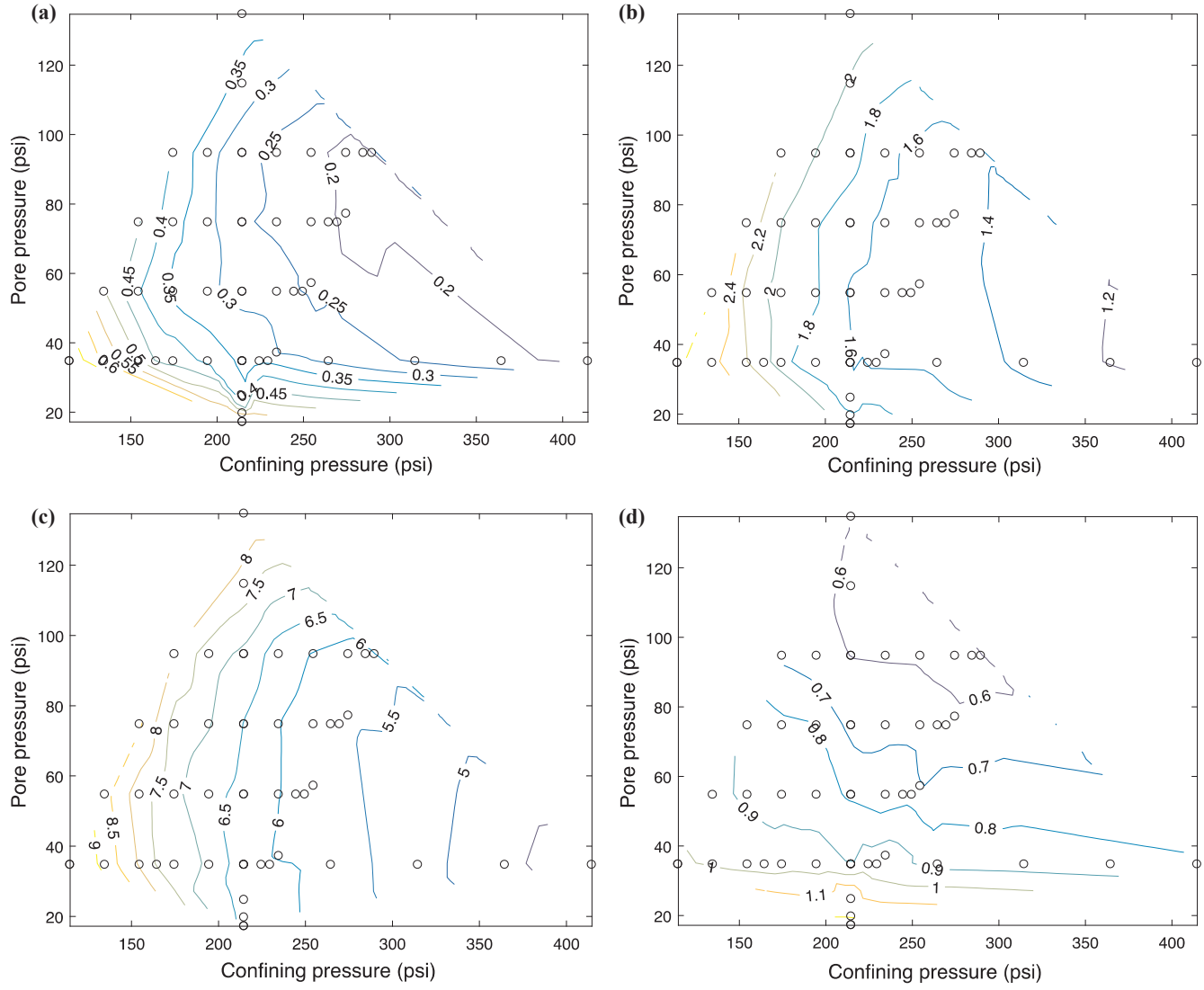

Fig. 4. Permeability contours for coal and sandstone sample (a. low permeable coal; b. medium permeable coal; c. high permeable coal; d. sandstone). Circles indicate the data points from which contours are determined.

samples are more influenced by confining pressure.

5.2. Knudsen number distribution and slip length analysis

To determine Knudsen number, we need to approximate the characteristic length scale for the coals (r_e) and the mean free path for gas (λ). The later is simply determined by Eq. (5). However, a single value for r_e may not exist since the structure of coal extends over many length scales. The resulting normalised pore size distribution (PSD) of the coals are presented in Fig. 5a, where the vertical axis is normalised frequency analysed using MIP in the range of $3.2\,\text{nm} \leq r_e \leq 50\,\mu\text{m}$. The MIP-based characteristic length controlling flow is described as the mean radius of the PSD truncated to pores below 100 nm because permeability is determined by large pore throats in a dual porosity system [46], which is displayed in Fig. 5b. Average values are reported in Table 1 along with bulk density and macro-porosity, which is defined as porosity of pores with aperture sizes greater than 100 nm. The high permeability coal has the greatest average aperture size while the medium permeability coal has the smallest aperture size. However, the porosity of the medium permeability coal is greater than the low permeability coal sample, which could explain the difference in permeability. Overall, the mercury data only provides an estimate of the relevant length scale and further analysis of trends between data sets is difficult due to the complex structure of coal. We also report r_e values estimated from Eq. (21) using experimental results near ambient conditions (effective stress = 80 psi). Overall we find that Eq. (21) can be used as an order of magnitude estimation of r_e when considering coal permeability.

The mean free path length for helium for all of the experiments using Eq. (5) is presented in Table 2. In addition, Fig. 6 provides a histogram of Knudsen numbers (Kn) for all experimental data using r_e from Eq. (21) and λ from Table 2. As a result, most of the experiments are within the range of Kn values where the first order slip boundary conditions proposed by Maxwell should be applicable. Besides, the Knudsen number for the sandstone experiments are on average greater than Kn for the coal experiments. For those data that have higher Knudsen number, a second or third order slip boundary condition may be required, as suggested by Karniadakis et al. [24].

Since the slip boundary condition applied in our capillary tube model should be valid for the range of Kn values tested, we can estimate slip lengths from the experimental data. It is generally accepted that when mean pore pressure is constant, the slip length will be constant. Therefore, we can plot r_e vs K_g/K_l under constant mean pore pressure. We then fit Eq. (16) to the experimental data using regression analysis to find the slip length (b_1). Fig. 7 provides data sets for the best and worst fits for slip length (b_1). It can be seen that the slip model fits the

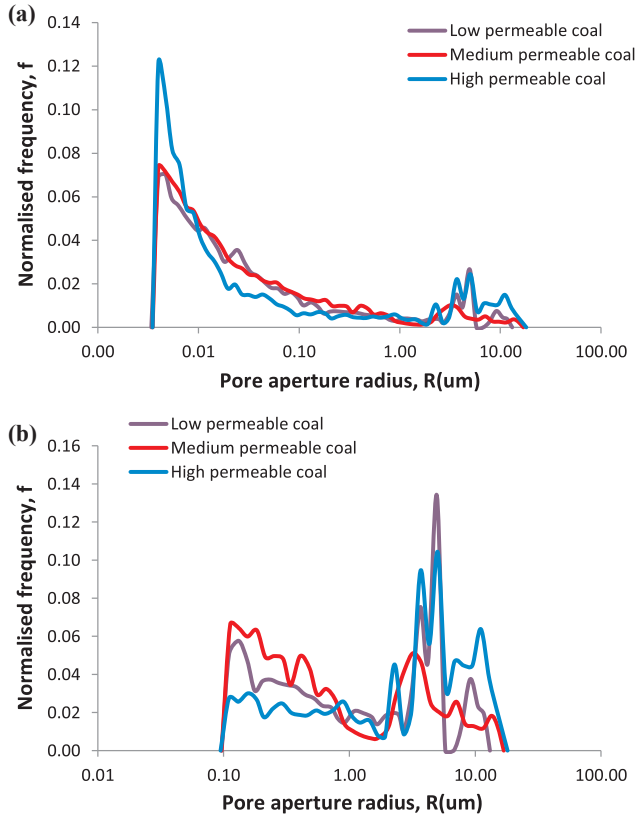

Fig. 5. PSD of the three coals calculated from MIP experiments (both normalised): (a) the complete PSD 3.2 nm ≤ d_p ≤ 60 μm; (b) a part of PSD, corresponding to meso- and macropores/fractures, d_p > 200 nm.

overall trends even for the case that provides the most error, which is for $Kn > 0.1$.

To systematically investigate the model, we plot the error for each data set versus slip length, as provided in Fig. 8. We define error in the regression model as the summation of the squared difference between the measured and predicted value. We observe that error becomes large when the slip length is greater than 90 nm, which corresponds to mean pore pressure less than 25 psig. At low mean pore pressure, Knudsen number is greater than 0.1. In Table 3 we provide the slip length and mean free path data for all of the experiments, which can be used in comparison to Fig. 8 where we plot b_1 versus error.

The relationship between mean free path length and slip length under different Knudsen numbers (Kn) is presented in Fig. 9. Based on Maxwell's model, solid walls are assumed as mathematically smooth, meaning that surface roughness of the boundary is not considered. However, Cao [3] demonstrated that roughness of a solid wall could affect the slip length, resulting in non-Maxwell behaviour were the slip length is no longer a linear function of mean free path. However, we observe a linear trend between b_1 and λ for all of the tested data sets. Even though the surface of coal pores/fractures are rough the influence of roughness on slip length is not observed in our experiments. It is seen in Fig. 8 that a liner trend is established with $R^2 = 0.95$. These results suggest that the applied first order boundary conditions for our experiments provide an appropriate approximation even though a few of

Table 2
Mean free path length of Helium under different mean pore pressure.

Effective stress	Mean pore pressure (psia)	λ (nm)
195	20	83
190	25	66
180	35	47
160	55	30
140	75	22
120	95	17
100	115	14
80	135	12

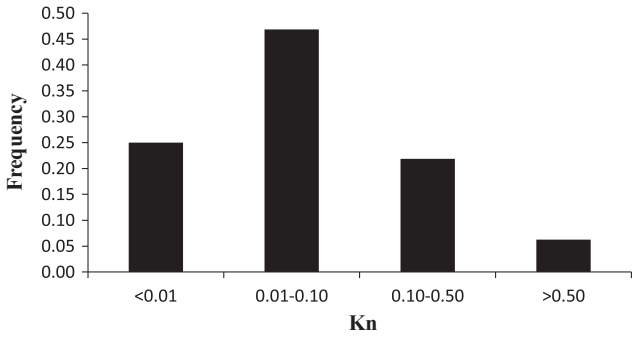

Fig. 6. Histogram of Knudsen numbers for all of the experiments.

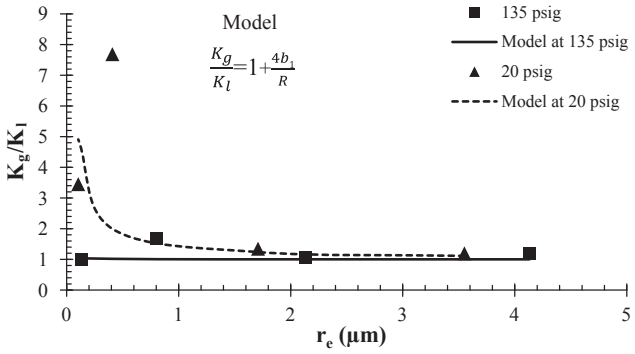

Fig. 7. Slip length estimation (Best fit at 135 psig and worst fit at 20 psig).

the data sets have $Kn > 0.1$.

In Fig. 10, we investigate the ratio of gas permeability to Klinkenberg corrected permeability for various Kn. The permeability ratio reflects the degree of slippage, i.e. a larger ratio implies greater rebound. As Knudsen number increases the slippage effect becomes increasingly obvious. At low Knudsen number ($Kn < 0.01$), the gas slippage is not obvious and the ratio between gas and Klinkenberg corrected permeabilities is nearly 1. However, for the range of Knudsen numbers of 0.01–0.1 the effect of gas slippage increases and when Knudsen number is greater than 0.1, the effect of slippage is significant. It should also be noted that the effect of matrix deformation is completely account for when dividing the gas permeability by Klinkenberg corrected permeability since the effect of permeability reduction with increasing effective stress is accounted for in the Klinkenberg corrected permeability measurements. This is clearly observed when comparing coal to

Table 1
Summary of samples properties determined from MIP experiments.

Sample/ID	Bulk density ρ_b (g/cc)	r_e MIP > 100 nm (μm)	Macro-porosity Φ^m (%)	r_e Eq. (21) (80 psi effective stress) (μm)
Low-permeability Coal	1.60	1.01	0.87	0.81
Medium-permeability Coal	1.34	0.69	1.10	2.13
High-permeability Coal	1.26	2.03	1.04	4.13

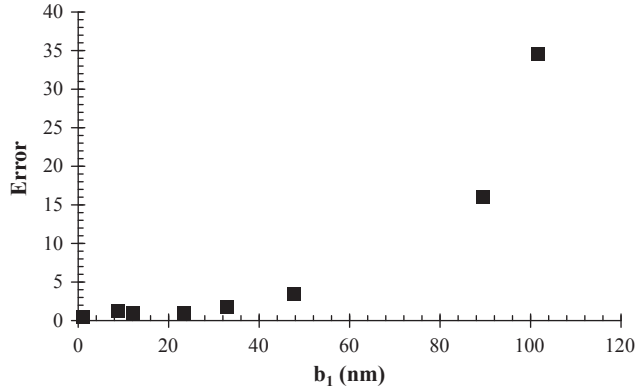

Fig. 8. The correlation between slip length and error from the regression analysis of Eq. (16) to the experimental data.

Table 3
Data of slip length (b_1) and mean free path length (λ) for all of the experiments.

Mean pore pressure (psig)	b_1 (nm)	λ (nm)
20	102	83
25	89	66
35	48	47
55	33	30
75	23	22
95	12	17
115	9	14
135	1	12

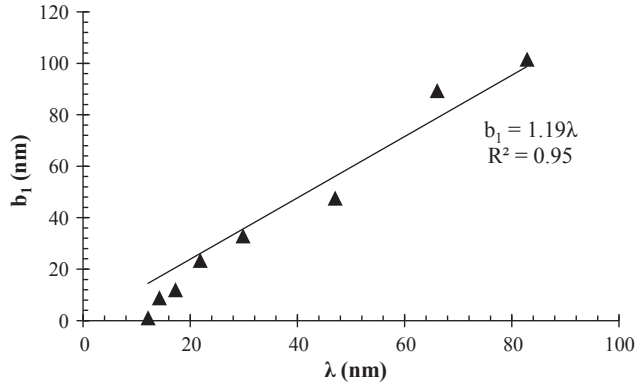

Fig. 9. Relationship between mean free path of gas and slip length under different Knudsen number.

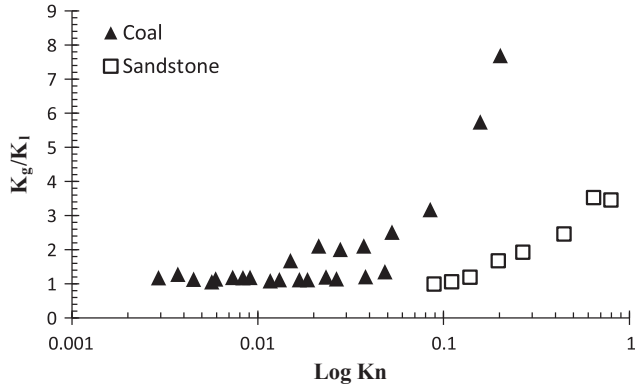

Fig. 10. Correlation between various Knudsen number and the ratio of gas permeability to Klinkenberg corrected permeability.

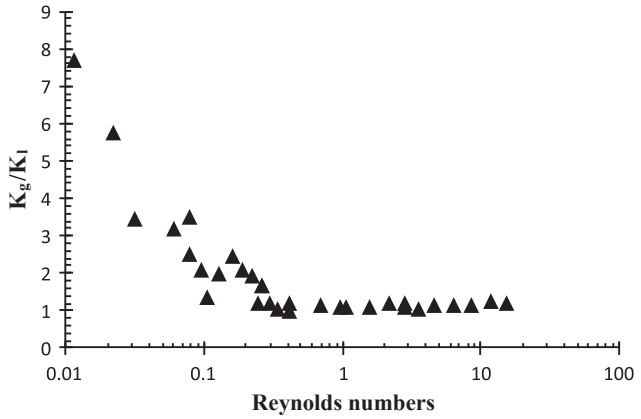

Fig. 11. Cross-plot between Reynolds numbers and K_g/K_l for all of the experimental data presented.

sandstone data. Sandstone is rigid and thus Klinkenberg corrected permeability does not decrease when effective stress increased. Therefore even though for large *Kn* the ratio of K_g/K_l is not as large as that for coal. This means that the gas slippage effect in coal is more obvious than sandstone at similar Knudsen number.

Overall, the proposed slippage model provides a reasonable explanation for permeability rebound with helium gas. With gas flow; however, high flow rates are possible leading to inertial effects, which could also have a large influence on coal permeability [15]. Forchheimer flow is known to occur for Reynolds numbers (*Re*) between 0.1 and 10 [60]. Fig. 11 provides a cross-plot between K_g/K_l and Reynolds numbers for all of the experiments. We observe that permeability rebound ($K_g/K_l > 1$) is measured for data sets where $Re < 0.1$. The cross-plot is not intended to demonstrate a trend between K_g/K_l and Reynolds numbers rather it demonstrates that Forchheimer flow can be neglected for most of the experimental data points and in particular for the data when slippage is the greatest, which we account for using the presented gas slippage model.

6. Conclusion

We measured gas and Klinkenberg corrected permeabilities for three coal samples with various permeabilities and one tight sandstone sample. By using inert helium gas for the experiments, we remove the mechanisms of swelling and shrinkage caused by gas sorption. Only gas slippage and mechanical deformation of cleats are considered and permeability rebound is evaluated within these constraints. The results demonstrated that higher permeable coal has less rebound than lower permeable coals. Also, rebound in the low permeable coal occurred at lower effective stress than high permeable coal. In addition, the Klinkenberg corrected permeabilities for all of the coal samples decreased with increasing effective stress.

A simple gas slippage model was developed using a first order boundary condition for slippage. Slip length (b_1) was estimated by fitting Eq. (20) to experimental data using regression analysis. As expected, slip length increases with decreasing mean pore pressure. The characteristic physical length scale was determined by permeability measurements and confirmed from MIP data. We demonstrated a linear relationship between b_1 and λ, as expected for low *Kn*. In particular, *Kn* is the key parameter for determining the extent of gas slippage, which can be estimate by using Eqs. (21) and (5) to approximate the relevant length scales. From this insight, we provided a correlation between Knudsen number (*Kn*) and permeability ratio (K_g/K_l) to describe the extent of gas slippage. Permeability rebound is more obvious in coal compared with sandstone under similar Knudsen number as coal is a more deformable medium.

In this paper, we describe permeability rebound based on the

correlation between effective stress and gas slippage by ignoring matrix shrinkage. Permeability rebound could be a significant process to enhance CBM recovery at the late stages of a coalbed life cycle. By considering these findings, permeability rebound by gas slippage can be more reliably detected/predicted for CBM reservoirs. In addition, our work can help those operators in CBM field understand when permeability rebound occurs and to what extent. Further studies are still required to characterise the additive effects of shrinkage and swelling on permeability rebound.

References

[1] Arabjamaloei R, Ruth D. Numerical study of inertial effects on permeability of porous media utilizing the Lattice Boltzmann Method. J Nat Gas Sci Eng 2017;44:22–36.
[2] Berg S, Cense AW, Hofman JP, Smits RMM. Two-phase flow in porous media with slip boundary condition. Transp Porous Media 2008;74(3):275–92.
[3] Cao BY. Non-Maxwell slippage induced by surface roughness for microscale gas flow: a molecular dynamics simulation. Mol. Phys. 2007;105(10):1403–10.
[4] Chapman S, Cowling TG. The mathematical theory of non-uniform gases: an account of the kinetic theory of viscosity, thermal conduction and diffusion in gases. Cambridge University Press; 1970.
[5] Chen Z, Pan Z, Liu J, Connell LD, Elsworth D. Effect of the effective stress coefficient and sorption-induced strain on the evolution of coal permeability: experimental observations. Int J Greenhouse Gas Control 2011;5(5):1284–93.
[6] Comisky CR, Wood JM, Burgis SE, Aquino SD, Freeman M. Nanopore-structure analysis and permeability predictions for a tight gas siltstone reservoir by use of low-pressure adsorption and mercury-intrusion techniques. SPE Reservoir Eval Eng 2012;15(6):648–61.
[7] Close JC. Natural fractures in coal; 1993 [chapter 5].
[8] Connell LD, Lu M, Pan Z. An analytical coal permeability model for tri-axial strain and stress conditions. Int J Coal Geol 2010;84(2):103–14.
[9] Cui X, Bustin RM. Volumetric strain associated with methane desorption and its impact on coalbed gas production from deep coal seams. AAPG Bull 2005;89(9):1181–202.
[10] De Gennes PG. Wetting: statics and dynamics. Rev Mod Phys 1985;57(3):827.
[11] de Gennes PG. On fluid/wall slippage. Langmuir 2002;18(9):3413–4.
[12] Deen WM. Analysis of transport phenomena; 1998.
[13] Dullien F. Porous media: fluid transport and pore structure. San Diego: Academic Press; 1992.
[14] Durucan S, Edwards JS. The effects of stress and fracturing on permeability of coal. Min. Sci. Technol. 1986;3(3):205–16.
[15] Forchheimer PH. Wasserbewegung durch boden. Zeitz Ver Duetch Ing 1901;45:1782–8.
[16] Gensterblum Y, Ghanizadeh A, Krooss BM. Gas permeability measurements on Australian subbituminous coals: fluid dynamic and poroelastic aspects. J Nat Gas Sci Eng 2014;19:202–14.
[17] Gray I. Reservoir engineering in coal seams: Part 1. The physical process of gas storage and movement in coal seams. SPE Reservoir Eng 1987;2(01):28–34.
[18] Harpalani S, Chen G. Gas slippage and matrix shrinkage effects on coal permeability. In: Proceedings of the 1993 international coal bed methane symposium. Tuscaloosa, AL, USA: University of Alabama; 1993.
[19] Harpalani S, Chen G. Influence of gas production induced volumetric strain on permeability of coal. Geotech Geol Eng 1997;15(4):303–25.
[20] Harpalani S, Schraufnagel RA. Shrinkage of coal matrix with release of gas and its impact on permeability of coal. Fuel 1990;69(5):551–6.
[21] Jasinge D, Ranjith PG, Choi SK. Effects of effective stress changes on permeability of latrobe valley brown coal. Fuel 2011;90(3):1292–300.
[22] Jing Y, Armstrong RT, Mostaghimi P. Rough-walled discrete fracture network modelling for coal characterisation. Fuel 2017;191:442–53.
[23] Jing Y, Armstrong RT, Ramandi HL, Mostaghimi P. Coal cleat reconstruction using micro-computed tomography imaging. Fuel 2016;181:286–99.
[24] Karniadakis G, Beskok A, Aluru N. Governing equations and slip models. Microflows Nanoflows Fundam Simul 2005:51–77.
[25] Klinkenberg LJ. The permeability of porous media to liquids and gases. Drilling and production practice. American Petroleum Institute; 1941.
[26] Laubach SE, Marrett RA, Olson JE, Scott AR. Characteristics and origins of coal cleat: a review. Int J Coal Geol 1998;35(1):175–207.
[27] Lauga E, Stone HA. Effective slip in pressure-driven Stokes flow. J Fluid Mech 2003;489:55–77.
[28] Levine JR. Model study of the influence of matrix shrinkage on absolute permeability of coal bed reservoirs. Geological Society, London, Special Publications 1996;109(1):197–212.
[29] Li J, Liu D, Yao Y, Cai Y, Chen Y. Evaluation and modeling of gas permeability changes in anthracite coals. Fuel 2013;111:606–12.
[30] Li YH, Lu GQ, Rudolph V. Compressibility and fractal dimension of fine coal particles in relation to pore structure characterisation using mercury porosimetry. Part Part Syst Charact 1999;16(1):25–31.
[31] Liu H-H, Rutqvist J. A new coal-permeability model: internal swelling stress and fracture–matrix interaction. Transp Porous Media 2010;82(1):157–71.
[32] Ma Q, Harpalani S, Liu S. A simplified permeability model for coalbed methane reservoirs based on matchstick strain and constant volume theory. Int J Coal Geol 2011;85(1):43–8.
[33] Maxwell JC. On stresses in rarified gases arising from inequalities of temperature. Philos Trans R Soc Lond 1879;170:231–56.
[34] Mitra A, Harpalani S, Liu S. Laboratory measurement and modeling of coal permeability with continued methane production: Part 1. Laboratory results. Fuel 2012;94:110–6.
[35] Mostaghimi P, Armstrong RT, Gerami A, Hu Y, Jing Y, Kamali F, et al. Cleat-scale characterisation of coal: an overview. J Nat Gas Sci Eng 2017;39:143–60.
[36] Navier CL. Memoir on the laws of fluid motion. Mem. Acad. Sci. (Paris) 1827;6:389.
[37] Nelson CR. Effects of geologic variables on cleat porosity trends in coalbed gas reservoirs. In: SPE/CERI gas technology symposium. Society of Petroleum Engineers; 2000.
[38] Okolo GN, Everson RC, Neomagus HW, Roberts MJ, Sakurovs R. Comparing the porosity and surface areas of coal as measured by gas adsorption, mercury intrusion and SAXS techniques. Fuel 2015;141:293–304.
[39] Palmer I, Mansoori J. How permeability depends on stress and pore pressure in coalbeds: a new model. In: SPE annual technical conference and exhibition. Society of Petroleum Engineers; 1996.
[40] Pan Z, Connell LD. Modelling permeability for coal reservoirs: a review of analytical models and testing data. Int J Coal Geol 2012;92:1–44.
[41] Pan Z, Connell LD, Camilleri M. Laboratory characterisation of coal reservoir permeability for primary and enhanced coalbed methane recovery. Int J Coal Geol 2010;82(3):252–61.
[42] Pattison CI, Fielding CR, McWatters RH, Hamilton LH. Nature and origin of fractures in Permian coals from the Bowen Basin, Queensland, Australia. Geol Soc Lond Spec Publ 1996;109(1):133–50.
[43] Pekot LJ, Reeves SR. Modeling the effects of matrix shrinkage and differential swelling on coalbed methane recovery and carbon sequestration. In: Paper 0328, Proc. 2003 international coalbed methane symposium. Citeseer: University of Alabama; 2003.
[44] Reiss LH. The reservoir engineering aspects of fractured formations. Editions Technip; 1980.
[45] Robertson EP, Christiansen RL. A permeability model for coal and other fractured, sorptive-elastic media. Idaho National Laboratory (INL); 2006.
[46] Ruth D, Lindsay C, Allen M. Combining electrical measurements and mercury porosimetry to predict permeability. Petrophysics 2013;54(06):531–7.
[47] Sawyer WK, Paul GW, Schraufnagel RA. Development and application of a 3-D coalbed simulator. In: Annual technical meeting. Petroleum Society of Canada; 1990.
[48] Scheidegger AE. The physics of flow through porous media; 1974.
[49] Seidle JP, Jeansonne MW, Erickson DJ. Application of matchstick geometry to stress dependent permeability in coals. In: SPE rocky mountain regional meeting. Society of Petroleum Engineers; 1992.
[50] Shi JQ, Durucan S. A model for changes in coalbed permeability during primary and enhanced methane recovery. SPE Reservoir Eval Eng 2005;8(04):291–9.
[51] Shi JQ, Durucan S. Drawdown induced changes in permeability of coalbeds: a new interpretation of the reservoir response to primary recovery. Transp Porous Media 2004;56(1):1–16.
[52] Somerton WH, Söylemezoğlu IM, Dudley RC. Effect of stress on permeability of coal. Int J Rock Mech Min Sci Geomech Abstr 1975. Elsevier.
[53] Terzaghi KV. Die berechnung der durchlassigkeitsziffer des tones aus dem verlauf der hydrodynamischen spannungserscheinungen. Sitzungsberichte der Akademie der Wissenschaften in Wien, Mathematisch-Naturwissenschaftliche Klasse, Abteilung IIa 1923;132:125–38.
[54] Tretheway DC, Meinhart CD. Apparent fluid slip at hydrophobic microchannel walls. Phys Fluids 2002;14(3):L9–12.
[55] Vinogradova OI. Drainage of a thin liquid film confined between hydrophobic surfaces. Langmuir 1995;11(6):2213–20.
[56] Wang G, Ren T, Wang K, Zhou A. Improved apparent permeability models of gas flow in coal with Klinkenberg effect. Fuel 2014;128:53–61.
[57] Wang K, Zang J, Wang G, Zhou A. Anisotropic permeability evolution of coal with effective stress variation and gas sorption: model development and analysis. Int J Coal Geol 2014;130:53–65.
[58] Washburn EW. The dynamics of capillary flow. Phys Rev 1921;17(3):273.
[59] Yamaguchi H, Matsuda Y, Niimi T. Tangential momentum accommodation coefficient measurements for various materials and gas species. J Phys Conf Ser 2012. IOP Publishing.
[60] Zeng Z, Grigg R. A criterion for non-Darcy flow in porous media. Transp Porous Media 2006;63(1):57–69.
[61] Zhu Y, Granick S. Limits of the hydrodynamic no-slip boundary condition. Phys Rev Lett 2002;88(10):106102.